



HAL
open science

Direct link between mechanical stability in gels and percolation of isostatic particles

Hideyo Tsurusawa, Mathieu Leocmach, John Russo, Hajime Tanaka

► **To cite this version:**

Hideyo Tsurusawa, Mathieu Leocmach, John Russo, Hajime Tanaka. Direct link between mechanical stability in gels and percolation of isostatic particles. 2018. hal-01901171v1

HAL Id: hal-01901171

<https://hal.science/hal-01901171v1>

Preprint submitted on 24 Oct 2018 (v1), last revised 29 Aug 2019 (v2)

HAL is a multi-disciplinary open access archive for the deposit and dissemination of scientific research documents, whether they are published or not. The documents may come from teaching and research institutions in France or abroad, or from public or private research centers.

L'archive ouverte pluridisciplinaire **HAL**, est destinée au dépôt et à la diffusion de documents scientifiques de niveau recherche, publiés ou non, émanant des établissements d'enseignement et de recherche français ou étrangers, des laboratoires publics ou privés.

Direct link between mechanical stability in gels and percolation of isostatic particles

Hideyo Tsurusawa,^{1†} Mathieu Leocmach,^{2†} John Russo,¹ Hajime Tanaka^{1*}

¹Department of Fundamental Engineering, Institute of Industrial Science, University of Tokyo,
4-6-1 Komaba, Meguro-ku, Tokyo 153-8505, Japan

²Univ Lyon, Université Claude Bernard Lyon 1, CNRS, Institut Lumière Matière,
F-69622, Villeurbanne, France

³School of Mathematics, University of Bristol, Bristol BS8 1TW, United Kingdom

† H.Tsurusawa and M.L. contributed equally to this work.

*To whom correspondence should be addressed; E-mail: tanaka@iis.u-tokyo.ac.jp.

October 3, 2018

Colloidal gels have unique mechanical and transport properties that stem from their bicontinuous nature, in which a colloidal network is intertwined with a viscous solvent, and have found numerous applications in foods, cosmetics, construction materials, and for medical applications, such as cartilage replacements. So far, our understanding of the process of colloidal gelation is limited to long-time dynamical effects, where gelation is viewed as a phase separation process interrupted by the glass transition. However, this picture does not address the emergence of mechanical stability. With confocal microscopy experiments, here we successfully follow the entire process of gelation with a single-particle resolution, yielding time-resolved measures of internal stress and viscoelasticity from the very beginning of the aggregation process. We observe that the network formed initially is not mechanically stable and undergoes rearrangements driven by self-generated internal stress, mechanically shaped. We show that mechanical metastability is reached only after isotropic percolation of locally isostatic environments, establishing a direct link between the load bearing ability of gels and the isostaticity condition. The emergence of mechanical stability due to isotropic percolation of isostatic structures leads to a transition from continuous liquid dynamics to intermittent solid dynamics.

Our work reveals the crucial roles of momentum conservation, or mechanical force balance, in gelation beyond the conventional purely out-of-equilibrium thermodynamic picture.

Introduction

Gels are soft solids composed of two intertwined phases: a solid network and a liquid solvent. They are an ubiquitous state of matter in every-day life, making up most of the foods we eat, the cosmetics we use, concretes, and our own organs. In colloidal gels, the network is composed of colloidal particles bonded together by attractive forces. Such colloidal assemblies are out of equilibrium, as the thermodynamic ground state of the system involves the macroscopic separation between a particle-rich (liquid) and a particle-poor (gas) phase. Despite the thermodynamic driving force towards compactness, the gel persists due to the dynamical arrest of the network, often described as a glass transition (1–8). This has led to the popular physical picture that a gel is formed by dynamical arrest of bicontinuous spinodal decomposition due to glass transition. The direct link between spontaneous gelation and spinodal decomposition has been carefully confirmed by combining experiments and theories (8). This recently established scenario is certainly a large step towards a more complete understanding of colloidal gelation.

However, this picture still leaves some fundamental problems unanswered: (i) The knowledge of ordinary spinodal decomposition predicts that the minority colloid-rich phase should form isolated clusters rather than the observed percolated network (9). (ii) A colloidal gel is sometimes formed by a network made of thin arms, which are too thin to be regarded as glasses. This casts some doubt on the popular scenario of dynamic arrest due to a glass transition. Indeed, the glass transition is defined as a kinetic transition and has no direct link to mechanical stability in a strict sense. Slow dynamics and mechanical stability are conceptually different. In an extreme case, for example, a gel formed by bonds with a short lifetime can be ergodic and in an equilibrium state. (iii) A gel often displays superdiffusive behavior, detected as the compressed exponential decay of a density correlation function, during aging, as observed by time-resolved spectroscopy techniques (10–12) and recently simulations (13–15). The origin of this phenomenon and its relation to problem (ii) are still elusive.

Several mechanisms have been proposed to try to rationalize some of these issues. Fluid momentum conservation can play an important role in phase separation of colloidal suspensions, giving to hydrodynamics an active role in network formation of the colloid-rich phase (4, 16). There have been some numerical studies on the role of hydrodynamics (17, 18) and mechanics (10, 13, 15, 19–21) in colloidal gelation. However, experimental investigations of these problems have been limited to observation of gels already formed (22, 23) due to the lack of a method to follow the whole kinetic processes with single-particle resolution in both space and time.

Moreover, some questions on the emergence of elasticity, which is the most fundamental physical property of gels, have still remained unanswered. It is well known that the isotropic percolation of a bond network is not sufficient to ensure mechanical stability (23–25). The sta-

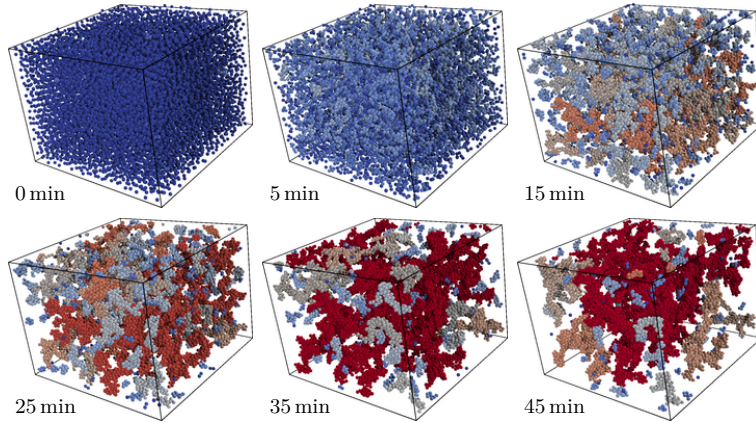


Figure 1: Snapshots from the entire gelation process reconstructed via particle-tracking of a typical sample close to the cluster-gel line ($\phi = 7.5\%$, $c_p = 1$ mg/g) using the salt-injection protocol. Particles are colored according to the size of the cluster they belong to, going from blue for monomers to red for the percolated cluster. See also Supplementary Movie 1.

bility of gels is ascribed to the formation of locally favored structures, or local energy-minimum configurations (26), while the mechanics of the network is being recognized to play a major role in the aging behavior of gels (13, 14, 27, 28). Purely geometrical conditions for mechanical stability have also been proposed. Whether a network is rigid can be determined using a pebble game algorithm (29), but this method is limited to 2D systems (30). A criteria on the average coordination number has been proposed (24) but has been recently invalidated (23). Kohl et al. (23) have found that in dilute suspensions, a final gel state is obtained only after directed percolation was observed, which differs from isotropic percolation by taking into account the directionality of the clusters. Hsiao et al. (31) have found that strain-induced yielding coincide with the loss of rigid clusters. Rigidity was defined using a local Maxwell criterion for isostaticity, that is 6 neighbors per particle (32). However, the relationship between local structures, dynamic arrest, and the emergence of elasticity remains poorly understood even at a fundamental level.

In order to address these problems, in this Article we study role of mechanics in colloidal gelation by dynamical confocal microscopy experiments. Various experimental protocols have been proposed to obtain reproducible gel structures, most of them involving shear (33–36), but here we use a protocol that does not involve external flow, and that allows us to observe the entire gelation process, from the beginning to the end with particle-level resolution. Our results point to the crucial role of isostatic structures, which are clusters of particles that, according to the Maxwell criteria of stability, have a number of neighbors equal to the number of degrees of freedom. We observe that the emergence of solidity coincides with the appearance of a system-spanning cluster of isostatic particles, i.e. with the isotropic percolation of isostatic particles. Both the glass transition and directed percolation are necessary conditions for the emergence of

mechanical metastability, but not sufficient conditions. In relation to this, we show that directed percolation and isotropic percolation of isostatic particles happen simultaneously only in dilute systems, while in concentrated systems the two time scales decouple, allowing us to link rigidity with the appearance of the system-spanning cluster of isostatic particles. These findings shed new light on the mechanisms of gel formation and coarsening, and also on the fate of gels.

Results

0.1 Phase separation dynamics observed at a single-particle level

0.1.1 System design

In our protocol, we first enclose a salt-free suspension of sterically and charge-stabilized colloids and non adsorbing polymers in a thin microscopy cell sketched in Supplementary Fig. S1. The bottom wall of the cell is an osmotic membrane providing contact with a long channel full of the same solvent mixture. Salt dissolution and subsequent migration of the ions along the channel and through the membrane induce screening of the electrostatic repulsion, revealing the depletion potential well due to the polymers. By contrast to similar designs used in our group and by others (37–39), here time needed for the ions to diffuse from the membrane across the cell thickness is of the same order of magnitude as the Brownian time of the particles $\tau_B = 10$ s. This relation between the two key timescales enables us to switch instantaneously (physically) from a long-range repulsive to a short-range attractive system without any external solvent flow. This causes uniform gelation starting from the homogeneous state, allowing *in situ* confocal microscopy observation throughout the process from a well-defined initial time, as shown in Fig. 1 and Supplementary Movie 1.

Here we stress that after the salt concentration is homogenized, our system can be regarded as a standard model for sticky hard-sphere systems. We confirmed this by comparing the experimental phase diagram with the one obtained with free volume theory for sticky hard spheres (Fig. 2).

0.1.2 Phase separation dynamics

In Fig. 2A, we show the phase diagram, where we can divide the state points into three regions based on the final state obtained by our protocol: at low polymer concentration ($c_p < 0.2$ mg/g) a sample fully relaxes to a fluid state; at very low colloid volume fraction ($\phi < 0.05$) and high polymer concentration the particles condense into long-lived well separated clusters as observed in (40); in the rest of the explored phase space we observe a long-lived space spanning network. In the phase diagram we also plot the spinodal (continuous) and the polymer overlap concentration (dashed) lines as obtained from free-volume theory calculations (41). Despite the limitations of the theory, the agreement between the spinodal line and our experiments is rather

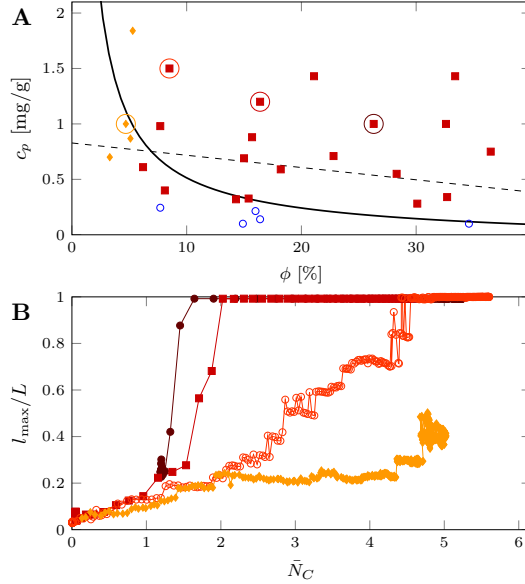


Figure 2: Different regimes of gelation. **(A)** Phase diagram. Experimental points are categorized based on the final state obtained in the reservoir cell. The spinodal line (solid curve) is obtained from free volume theory in polymer dilute regime. The dashed line is the polymer overlap concentration in the free volume. State points analyzed in **(B)** are circled. **(B)** Comparison of system evolution in terms of largest cluster extent (l_{\max}/L) and of mean coordination number (\bar{N}_C). Symbols \blacklozenge , \circ , \blacksquare and \bullet correspond to $(\phi, c_p)=(4.2\%, 1\text{ mg/g})$, $(8\%, 1.5\text{ mg/g})$, $(16\%, 1.2\text{ mg/g})$, and $(27\%, 1\text{ mg/g})$, respectively.

satisfactory, with the only exception being the region of small colloidal volume fractions and high polymer concentration (see, e.g., Ref. (8)).

We confirm in Supplementary Materials that the phase separation kinetics follows arrested spinodal behavior both in the cluster phase and in the percolating samples. We also confirm in Supplementary Materials the crucial role of hydrodynamics in facilitating percolation.

To characterize the gelation path in real space, we compute the instantaneous mean number of neighbors \bar{N}_C , or coordination number, that quantifies the compactness of the structure. We also compute the spatial extent of the largest cluster l_{\max} that we normalize by the size of the field of view L to obtain a measure of the distance to isotropic percolation of the system. Figure 2B shows a system trajectory in the $(l_{\max}/L, \bar{N}_C)$ plane for various colloidal volume fractions ϕ . All trajectories show a linear increase of both cluster size l_{\max}/L and number of neighbors \bar{N}_C at early times. This is followed by the coarsening stage, which happens differently depending on the density. At high ϕ , coarsening occurs after percolation, which happens within the first few τ_B after charge screening by salt. At low ϕ , percolation never takes place and coarsening results in the compaction of individual clusters, that keeps their overall size l_{\max}/L , while increasing the number of neighbors \bar{N}_C , see Supplementary Fig. S4. We did not observe any Ostwald ripening

among clusters, indicating that the diffusive evaporation-condensation coarsening mechanism is negligible compared to cluster collisions and coalescence, as expected for colloidal viscoelastic phase separation (16). At intermediate densities, we observe the process detailed in Fig. 1: formation of low-compacity clusters that then slowly connect together to build the percolating network. This process can take hundreds of τ_B and is competing with cluster compaction, as indicated by the oblique trajectory (red open circles) in Fig. 2B. Particle-level quantities thus demonstrate that the path to gelation is not universal and depends on the colloid volume fraction even within the gelation region. By contrast, polymer concentration, i.e. the depth of the attraction potential, has little effect on the path to gelation, see Supplementary Fig. S6.

In section 0.2, we will explore the precise mechanism of arrest and the emergence of mechanical rigidity by studying the dynamics within the network of percolating samples.

0.2 Emergence of mechanical stability

0.2.1 Percolation

As already noted by Kohl et al. (23), the average coordination number \bar{N}_C is a poor predictor of dynamical arrest, as we confirm in Supplementary Fig. S5. In this section we examine the different percolation time-scales, and their relation with the emergence of solidity in the samples.

Isotropic percolation is related to the appearance of a system-spanning network, and can be determined by looking at the time evolution of the largest connected cluster l_{\max} , as plotted in Fig. 3A and B (orange curves). The isotropic percolation time (τ_{IT}^{all}) is then defined as the moment when $l_{\max} > 0.95L$. We checked that our field of view is large enough not to suffer from finite size effects.

Directed percolation is related to the appearance of a directed path that spans the whole system. A directed path is defined as a path with no loop or turning back, such that every step is in either the positive X, Y, or Z directions. The maximum spatial extent of directed paths l_D is plotted in Fig. 3A and B (orange symbols). We thus define the *directed percolation* time (τ_D^{all}) as the moment when $l_D > 0.95L$.

The concepts of isotropic and directed percolation can also be applied to a subset of particles. In particular, we focus here on isostatic particles, which are particles that have at least six bonded neighbors. For isostatic clusters we plot in Fig. 3A and B both l_{\max} (purple curves) and l_D (purple symbols) (see also Supplementary Movie 2). The isotropic percolation time of isostatic particles is τ_{IT}^{IS} .

Fig. 3A and B show the time evolution of the clusters in the dilute ($\phi = 8\%$) and dense suspensions ($\phi = 21\%$) respectively. We observe that directed percolation of all particles and isotropic percolation of isostatic particles occur simultaneously in the dilute regime, $\tau_D^{\text{all}} \sim \tau_{IT}^{\text{IS}}$. However the two time scales are well separated in the dense regime, $\tau_D^{\text{all}} \ll \tau_{IT}^{\text{IS}}$. This separation of time scales offers the opportunity to test the role of both type of space spanning microstructures in the mechanical stability of gels.

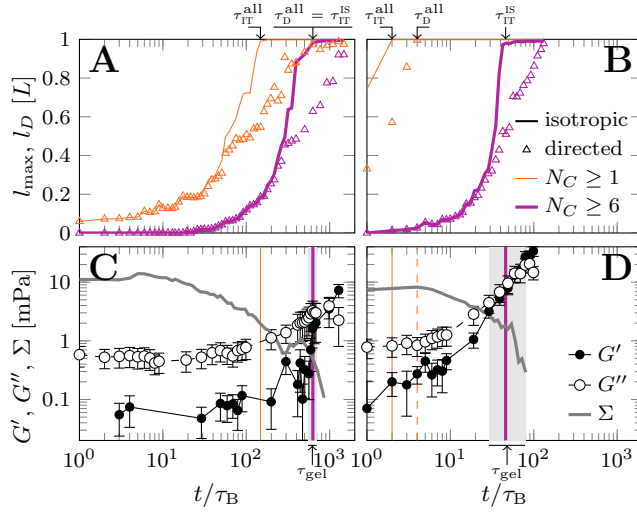


Figure 3: Evolution of space-spanning microstructure and mechanical response. (A) and (B): Percolation processes, for a dilute ($\phi = 8\%$, $c_p = 1.5$ mg/g) and a dense ($\phi = 27\%$, $c_p = 1$ mg/g) sample. The processes of isotropic and directed percolation of all particles ($N_C \geq 1$) are respectively plotted as thin orange curve and orange symbols. The processes of isotropic and directed percolation of isostatic particles ($N_C \geq 6$) are respectively plotted as thick purple curve and purple symbols. (C) and (D): Mechanical response for the same samples. Elastic (G') and viscous (G'') shear moduli at the highest available frequency ($f = 0.1\tau_B^{-1}$), obtained by two-particle microrheology, are drawn respectively as filled and open circles. The thick grey curve is the internal stress Σ obtained from the measure of bond-breaking probability. The thin orange and thick purple vertical lines show the isotropic percolation times for all particles (τ_{IT}^{all}) and isostatic particles (τ_{IT}^{is}) respectively. The orange dashed vertical line in (D) shows the directed percolation time for all particles (τ_D^{all}). The gray vertical band shows the possible range of mechanical gelation time τ_{gel} (see Supplementary Materials).

0.2.2 Mechanical stability and percolations

The solid nature of a material is most often defined from linear mechanical response. For colloidal gels, however, mechanical stability cannot be predicted without an understanding of internal stresses (14). Here we are able to extract both information from our particle-level experiments. We use the particles themselves as passive microrheological probes to extract the elastic (G') and viscous (G'') parts of the shear modulus, see Supplementary Materials. Microrheology is a transformation (generalized Stokes-Einstein relation) applied on the (two-point) mean square displacement (42). It thus relates dynamical measurements with linear viscoelasticity. In particular, observing $G' > G''$ for a given frequency indicates the emergence of elasticity, or dynamical arrest, at the corresponding time scale. We denote this time as τ_{gel} , the gelling time (see Supplementary Materials for a more accurate definition and a discussion on

uncertainties). We also extract the average value of the internal stress Σ from the bond breaking rate, see Supplementary Materials. Results are shown in Fig. 3C and D for direct comparisons with the microstructure.

The typical ranges of stresses and moduli we measure extend below 0.1 mPa, well below sensitivity of conventional rheometers. That is why previous microscopic studies on the mechanics of colloidal gels have been restricted to the comparison of the structure before and after a large amplitude shear flow with no simultaneous measure of the stress response (31, 34, 43). From Fig. 3C and D we see that, as expected, all samples are purely viscous at short times, with a value of G'' consistent with the viscosity of a hard sphere suspension at their respective volume fractions. Internal stresses are high at short time, reflecting the stretching of the network, which is formed by hydrodynamic interactions in a mechanically frustrated state. The emergence of mechanical stability is captured simultaneously from both the linear viscoelasticity measurements, with the crossing between G' and G'' , and the internal stress, which is accompanied by a sharp drop in Σ . The timing of the emergence of elasticity is thus unambiguous (vertical gray zone in Fig. 3C and D) and occurs well after isotropic percolation time τ_{IT}^{all} (see orange vertical lines in Fig. 3C and D). We also find no special value of \bar{N}_C at that time, see Supplementary Fig. S5. This generalizes observations by Kohl et al. (23) on the final state of dilute samples (see Supplementary Materials).

In dilute samples, the elastic behavior occurs in the same time scale as directed percolation of all particles. However, isotropic percolation of isostaticity also occurs simultaneously, $\tau_D^{\text{all}} \sim \tau_{IT}^{\text{IS}} \sim \tau_{\text{gel}}$. Therefore we have to look at the dense regime to disentangle the two possible microstructural causes. Indeed in the dense regime the elastic behavior emerges around $\tau_{\text{gel}} \sim 45\tau_B$ well after directed percolation of all particles taking place at $\tau_D^{\text{all}} \sim 4\tau_B$. Thus, directed percolation is not *in general* a sufficient condition to obtain mechanical stability. However, we observe systematically that elasticity emerges in the same time scale as isotropic percolation of isostaticity, $\tau_D^{\text{all}} \ll \tau_{IT}^{\text{IS}} \sim \tau_{\text{gel}}$, (see thick purple vertical lines fall inside gray vertical zone in Fig. 3C and D). Directed percolation of isostaticity (purple symbols in Fig. 3A and B) always occurs at later times and does not seem to play an important role. This allows to lay the main result of this article: the emergence of rigidity is caused by isotropic percolation of isostatic clusters, able to bear stress across the sample. We show below why the isotropic percolation of isostatic particles occurs at the same time as directed percolation in the dilute regime, while being decoupled from it at higher volume fractions.

0.2.3 Directed or isostaticity percolations

In Fig. 4A, we compare across all our experiments the time to percolation of isostaticity τ_{IT}^{IS} ($\sim \tau_{\text{gel}}$) to the time to directed percolation τ_D^{all} . We confirm that at high volume fractions, typically $\phi > 14\%$, the two types of percolation phenomena are decoupled, with $2 < \tau_{IT}^{\text{IS}}/\tau_D^{\text{all}} < 20$ depending on the state point. By contrast at lower ϕ , both percolations occur simultaneously, independently of the attraction strength.

The reason for this coincidence can be understood by the specific path to gelation in the

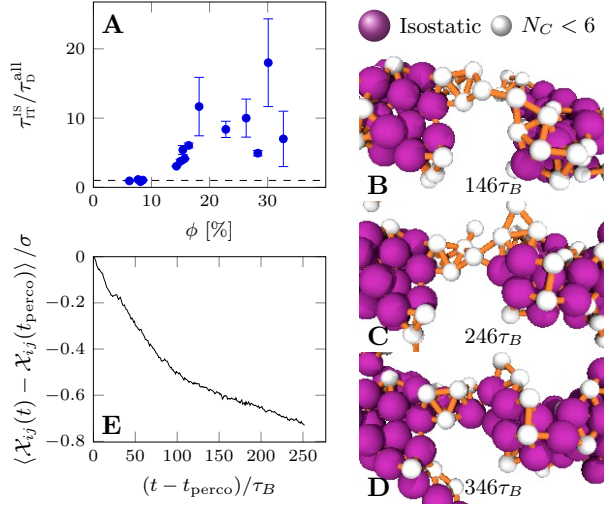


Figure 4: Directed percolation and isostaticity percolation. **(A)** Ratio of the time of isostaticity percolation τ_{IT}^{IS} to that of directed percolation τ_D^{all} , as a function of colloid volume fraction. Horizontal dashed line shows when both times are equal. **(B)** Detail of a reconstruction from confocal coordinates around the percolation time in a dilute sample ($\phi = 8\%$, $c_p = 1.5$ mg/g). Isostatic particles are drawn to scale, non-isostatic ones are drawn smaller for clarity. The bond network is displayed in orange. **(C)** and **(D)**: Same as **(B)** at later times. **(E)** Increment of Euclidean distance between two isostatic clusters, averaged over all such pairs initially connected by a non-isostatic network strand. The reference time is the percolation time t_{perco}

dilute regime. We have seen in Fig. 2C that isotropic percolation occurs at a late stage, when the clusters have already become compact by squeezing out the solvent to form isostatic structures. Indeed, Fig. 3A shows that at the percolation time ($\tau_{IT}^{all} \sim 1.5 \times 10^2 \tau_B$), isostatic particles already form clusters that reach up to a tenth of the observation window L . Cluster-size distribution (see Supplementary Fig. S11) and three dimensional reconstruction in Fig. 4B show that these isostatic clusters around the percolation time are compact, typically 3 to 5 particles in diameter and linked by non-isostatic bridges. The floppiness of these bridges prevents directed paths to reach percolation.

From this situation, percolation of isostaticity proceeds by the compaction of the floppy bridges. Importantly, this compaction takes place without adsorption of new particles onto the bridge. Compaction is a local process that involves no particle migration but only creation of new bonds, as shown in Fig. 4B-D. Consistently, this compaction leads to a straightening and a shortening of the strands. We quantify this shortening by computing the Euclidean distance $\mathcal{X}_{ij}(t)$ between the centers of mass of two isostatic clusters i and j . The increment of this distance as a function to the time distance to the percolation, averaged over all cluster pairs connected by a floppy bridge, is shown on Fig. 4E. The observed shortening is about 0.7σ or

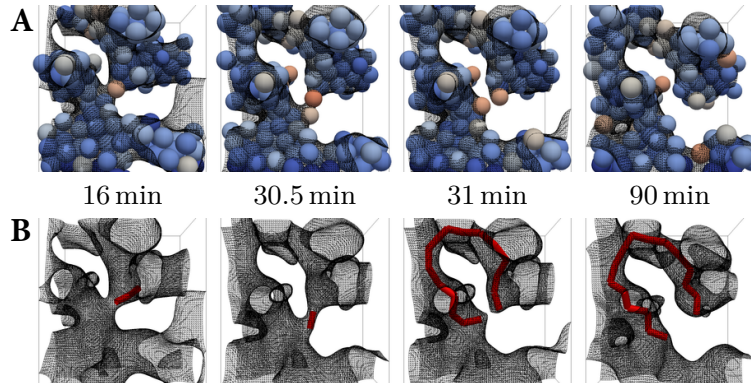


Figure 5: Breakup of the network by internal stress. **(A)** Reconstruction from experimental coordinates ($\phi = 29\%$, $c_p = 0.7\text{ mg/g}$) of strand rupture event. Particles are drawn to scale and colored by a measure of two-fold symmetry q_2 (see Supplementary Materials on its definition) from blue (low) to red (high). We note that q_2 is a measure of the degree of local stretching. **(B)** Same event from a topological point of view. The red line indicates the shortest on-graph path between the two particles of interest, whose drastic change clearly indicates the breakup event. The meshed surface is a Gaussian coarse-graining of the network pattern.

25% of the initial length. Directed percolation becomes possible only when a percolating path has become straight enough, which implies isostaticity. That is why directed percolation and isostaticity percolation occur simultaneously in the dilute regime. The simultaneity of directed percolation and emergence of rigidity in the dilute regime is thus a coincidence mediated by isotropic percolation of already isostatic clusters, in which the two different types of percolation can take place at the same time. In other words, the emergence of rigidity in gels should not be linked to the universality class of directed percolation.

0.2.4 Stress-induced network breakup

In a dense system, after directional percolation of all particles, the number of nearest neighbors monotonically increases to minimize the energy of the structure (mainly the interfacial energy cost), resulting in the growth of isostatic configurations, as discussed above. During this process the mechanical tension internal to the network grows, driving it towards compaction, which can lead to network coarsening accompanying bond breakage (see Fig. 5A and B). Unlike in simulations (13), we cannot directly measure the local internal stress at this moment, but we can still see its effects through the local stretching measured by the degree of two-fold symmetry q_2 (see the particle color in Fig. 5A). From this, we may say that a bond breakage event is the consequence of stress concentration on a weak bond, leading to local stretching of the bond, and its eventual breakup. In other words, mechanical stress acts against diffusive particle aggregation (or compaction), which is the stress-diffusion coupling characteristic of phase separation in

dynamically asymmetric mixtures (4, 16). This stress-driven aging is accompanied by mechanical fracture of the percolated network structure by the self-generated mechanical stress. The mechanical stability can be attained only after the formation of a percolated isostatic structure, which is a necessary and sufficient condition for a structure to be mechanically stable. When the percolated isostatic structure can support the internal stress everywhere, the system can attain mechanical stability.

Discussion

In summary, we have observed with particle-level resolution the entire process of gelation from the very beginning to the final arrested state at various state points for the first time. The early stages are characterized by the universal features of spinodal decomposition, with clusters emerging with a constant wave vector (in Supplementary Materials we show also that hydrodynamic interactions hinder the formation of isolated compact clusters, leading to the formation of a percolated network, and give to the coarsening process a non-universal behavior). At high volume fractions, elongated structures immediately percolate into a thin, mechanically unstable network that undergoes stress-driven rearrangements enabling the formation of locally isostatic structures that finally percolate. At low volume fractions, percolation is delayed, thus initially elongated clusters have the time to compact before eventually connecting into a percolating structure. Isostatic clusters thus already exist at percolation time but are linked by floppy strands that have to compact to induce isostaticity percolation. Microrheological information reveals that the general mechanism responsible for mechanical solidity, which is signaled by the dominance of elastic over viscous modulus, is neither isotropic percolation nor directed percolation, but instead the isotropic percolation of isostatic structures.

The picture of gelation that emerges from our observations is far more rich than previously understood, and suggests that mechanical stability plays a fundamental role in addition to dynamical arrest. The glass transition is kinetically defined as the point above which the relaxation time is slower than the observation time, whereas mechanical stability is acquired with the percolation of isostaticity. Thus, we argue that a key feature of gelation is the arrest *by isostaticity percolation* of a viscoelastic spinodal decomposition. Then, the mechanical stability of a gel is determined by a competition between the yield stress of the isostaticity network and the internal stress towards network shrinking produced by the interface free-energy cost. Since a gel is not in an equilibrium state and the stress can be concentrated in a weak part of the network, perfect mechanical stability may never be attained, resulting in slow aging via either surface diffusion or bond breakage.

An understanding based on the mechanical equilibrium and isostaticity might pave the way to a more operative description of colloidal gels, and allow complex issues to be addressed in terms of mechanics and rheology. For example, stress-driven aging plays a fundamental role in the formation of porous crystals (39). The spontaneous delayed collapse of colloidal gels (44, 45) could be viewed as the final overcome of the mechanical frustration. Under small

stresses also a delayed yielding is observed (46–48). Despite a sustained attention, the yielding process of colloidal gels still lacks a general consensus. For instance we do not know why some colloidal gels display a yield stress fluid behavior, that is a reversible yielding and no fracture (46, 49), whereas others display a brittle solid behavior with the irreversible opening of fractures (48). Understanding colloidal gels as a both non-ergodic and mechanically stabilized state of matter may help solving these issues.

Supplementary Material accompanies this paper at <http://www.scienceadvances.org/>.

Materials and Methods

We use colloidal particles made of poly(methyl methacrylate) copolymerized with 25 kDa methacryloxypropyl terminated poly(dimethyl siloxane) (Gelest) for steric stabilisation (50), with 2 % of methacrylic acid to allow electrostatic repulsion, and with (rhodamine isothiocyanate)-aminostyrene for fluorescent labeling (51). Particles (diameter $\sigma = 2.75 \mu\text{m}$ estimated from direct confocal measurements (52, 53)) are dispersed in a mixture of cis-decalin (Tokyo Kasei) and bromocyclohexane (Sigma-Aldrich) that matches both optical index and density of the colloids. To induce short-ranged depletion attraction, we use 8.4 MDa polystyrene (TOSOH) as non-adsorbing polymer. We estimate the radius of gyration to $R_g = 148 \text{ nm}$, leading to an attraction range of $1.10(6)\sigma$. In the absence of salt, the Debye length reaches several μm and the (weakly) charged colloids experience a long range electrostatic repulsion (54).

We enclose this suspension in a thin (200 μm) microscopy cell sketched in Supplementary Fig. S1. The bottom wall of the cell is an osmotic membrane providing contact with a long channel full of the same solvent mixture. At the beginning of the experiment, we introduce solid tetrabutylammonium bromide (Fluka) into the channel and start data acquisition within 30 s. This salt injection screens the electrostatic interactions between colloids. Thus, after the salt injection, the colloid system can be regarded as sticky hard spheres.

We collect the data on a Leica SP5 confocal microscope, using 532 nm laser excitation. We control the temperature of both stage and objective lens, allowing a density matching of the order of 10^{-4} between particles and solvent, enough to observe the late stage of gelation with little influence of gravity despite our large particle size (gravitational Peclet number $\text{Pe} < 10^{-6}$). We track the particle coordinates in three dimensions (3D) with an accuracy of around 0.03σ (55). We consider two particles bonded when their distance is shorter than the first minimum of $g(r)$, i.e. $3.55 \mu\text{m}$. This defines the bond graph that we analyze using NetworkX library (56). The precise choice of this distance does not affect significantly our results, in particular percolation times.

References

1. R. Piazza, G. D. Pietro, Phase Separation and Gel-like Structures in Mixtures of Colloids and Surfactant. *Europhys. Lett.* **28**, 445–450 (1994).

2. H. Verduin, J. K. G. Dhont, Phase diagram of a model adhesive hard-sphere dispersion. *J. Colloid Interf. Sci.* **172**, 425–437 (1995).
3. N. a. Verhaegh, J. S. van Duijneveldt, J. K. Dhont, H. N. Lekkerkerker, Fluid-fluid phase separation in colloid-polymer mixtures studied with small angle light scattering and light microscopy. *Physica A* **230**, 409–436 (1996).
4. H. Tanaka, Viscoelastic model of phase separation in colloidal suspensions and emulsions. *Phys. Rev. E* **59**, 6842–52 (1999).
5. V. Trappe, V. Prasad, L. Cipelletti, P. N. Segre, D. A. Weitz, Jamming phase diagram for attractive particles. *Nature* **411**, 772–775 (2001).
6. W. C. Poon, The physics of a model colloid polymer mixture. *J. Phys.: Condens. Matter* **14**, R859-R880 (2002).
7. F. Cardinaux, T. Gibaud, A. Stradner, P. Schurtenberger, Interplay between spinodal decomposition and glass formation in proteins exhibiting short-range attractions. *Phys. Rev. Lett.* **99**, 118301 (2007).
8. P. J. Lu, E. Zaccarelli, F. Ciulla, A. B. Schofield, F. Sciortino, D. A. Weitz, Gelation of particles with short-range attraction. *Nature* **453**, 499–503 (2008).
9. A. Onuki, *Phase Transition Dynamics* (Cambridge Univ. Press, Cambridge,, 2002).
10. L. Cipelletti, S. Manley, R. C. Ball, D. A. Weitz, Universal Aging Features in the Restructuring of Fractal Colloidal Gels. *Phys. Rev. Lett.* **84**, 2275–2278 (2000).
11. L. Ramos, L. Cipelletti, Ultraslow Dynamics and Stress Relaxation in the Aging of a Soft Glassy System. *Phys. Rev. Lett.* **87**, 245503 (2001).
12. B. Ruta, O. Czakkel, Y. Chushkin, F. Pignon, R. Nervo, F. Zontone, M. Rinaudo, Silica nanoparticles as tracers of the gelation dynamics of a natural biopolymer physical gel. *Soft Matter* **10**, 4547 (2014).
13. H. Tanaka, T. Araki, Spontaneous coarsening of a colloidal network driven by self-generated mechanical stress. *Europhys. Lett.* **79**, 1–6 (2007).
14. M. Bouzid, J. Colombo, L. V. Barbosa, E. Del Gado, Elastically driven, intermittent microscopic dynamics in soft solids. *Nature Commun.* **8**, 1–8 (2016).
15. P. Chaudhuri, L. Berthier, Ultra-long-range dynamic correlations in a microscopic model for aging gels. *Phys. Rev. E* **95**, 060601 (2017).
16. H. Tanaka, Viscoelastic phase separation. *J. Phys.: Condens. Matter* **12**, R207-R264 (2000).

17. A. Furukawa, H. Tanaka, Key Role of Hydrodynamic Interactions in Colloidal Gelation. *Phys. Rev. Lett.* **104**, 245702 (2010).
18. Z. Varga, G. Wang, J. W. Swan, The hydrodynamics of colloidal gelation. *Soft Matter* **11**, 9009–9019 (2015).
19. J. Colombo, E. Del Gado, Self-assembly and cooperative dynamics of a model colloidal gel network. *Soft matter* **10**, 4003–15 (2014).
20. V. Testard, L. Berthier, W. Kob, Intermittent dynamics and logarithmic domain growth during the spinodal decomposition of a glass-forming liquid. *Journal of Chemical Physics* **140** (2014).
21. R. N. Zia, B. J. Landrum, W. B. Russel, A micro-mechanical study of coarsening and rheology of colloidal gels: Cage building, cage hopping, and Smoluchowski’s ratchet. *J. Rheol.* **58**, 1121–1157 (2014).
22. C. P. Royall, J. Eggers, A. Furukawa, H. Tanaka, Probing Colloidal Gels at Multiple Length Scales: The Role of Hydrodynamics. *Phys. Rev. Lett.* **114**, 258302 (2015).
23. M. Kohl, R. F. Capellmann, M. Laurati, S. U. Egelhaaf, M. Schmiedeberg, Directed percolation identified as equilibrium pre-transition towards non-equilibrium arrested gel states. *Nature Commun.* **7** (2016).
24. N. E. Valadez-Pérez, Y. Liu, A. P. R. Eberle, N. J. Wagner, R. Castañeda-Priego, Dynamical arrest in adhesive hard-sphere dispersions driven by rigidity percolation. *Phys. Rev. E* **88**, 1–5 (2013).
25. J. J. Richards, J. B. Hipp, J. K. Riley, N. J. Wagner, P. D. Butler, Clustering and Percolation in Suspensions of Carbon Black. *Langmuir* **33**, 12260–12266 (2017).
26. C. P. Royall, S. R. Williams, T. Ohtsuka, H. Tanaka, Direct observation of a local structural mechanism for dynamic arrest. *Nature Mater.* **7**, 556–561 (2008).
27. J. P. Bouchaud, E. Pitard, Anomalous dynamical light scattering in soft glassy gels. *Eur. Phys. J. E* **9**, 287–291 (2002).
28. L. Cipelletti, L. Ramos, S. Manley, E. Pitard, D. A. Weitz, E. E. Pashkovski, M. Johansson, Universal non-diffusive slow dynamics in aging soft matter. *Faraday Discuss.* **123**, 237–251 (2003).
29. D. J. Jacobs, M. F. Thorpe, Generic Rigidity Percolation: The Pebble Game. *Physical Review Letters* **75**, 4051–4054 (1995).
30. S. Zhang, L. Zhang, M. Bouzid, D. Z. Rocklin, E. Del Gado, X. Mao, Correlated rigidity percolation and colloidal gels (2018).

31. L. C. Hsiao, R. S. Newman, S. C. Glotzer, M. J. Solomon, Role of isostaticity and load-bearing microstructure in the elasticity of yielded colloidal gels. *Proc. Natl. Acad. Sci. USA* **109**, 16029–34 (2012).
32. J. C. Maxwell, On the calculation of the equilibrium and stiffness of frames. *Phil. Mag. A* **27**, 294–299 (1864).
33. C. O. Osuji, C. Kim, D. A. Weitz, Shear thickening and scaling of the elastic modulus in a fractal colloidal system with attractive interactions. *Physical Review E* **77**, 060402 (2008).
34. S. B. Lindström, T. E. Kodger, J. H. B. Sprakel, D. A. Weitz, Structures, stresses, and fluctuations in the delayed failure of colloidal gels. *Soft Matter* **8**, 3657 (2012).
35. N. Koumakis, E. Moghimi, R. Besseling, W. C. Poon, J. F. Brady, G. Petekidis, Tuning colloidal gels by shear. *Soft Matter* **11**, 4640–4648 (2015). Citation Key: Koumakis2015.
36. E. Moghimi, A. Jacob, N. Koumakis, G. Petekidis, Colloidal Gels Tuned by Oscillatory Shear. *Soft Matter* (2017).
37. H. Tanaka, Y. Nishikawa, T. Koyama, Network-forming phase separation of colloidal suspensions. *Journal of Physics: Condensed Matter* **17**, L143–L153 (2005). Citation Key: Tanaka2005f.
38. J. Sato, V. Breedveld, Transient rheology of solvent-responsive complex fluids by integrating microrheology and microfluidics. *Journal of Rheology* **50**, 1–19 (2006).
39. H. Tsurusawa, J. Russo, M. Leocmach, H. Tanaka, Formation of porous crystals via viscoelastic phase separation. *Nature Materials* **16**, 1022–1028 (2017).
40. P. J. Lu, J. C. Conrad, H. M. Wyss, A. B. Schofield, D. A. Weitz, Fluids of clusters in attractive colloids. *Phys. Rev. Lett.* **96**, 028306 (2006).
41. G. J. Fleer, R. Tuinier, Analytical phase diagrams for colloids and non-adsorbing polymer. *Adv. Colloid Interface Sci.* **143**, 1–47 (2008).
42. J. C. Crocker, M. T. Valentine, E. R. Weeks, T. Gisler, P. D. Kaplan, A. G. Yodh, D. A. Weitz, Two-Point Microrheology of Inhomogeneous Soft Materials. *Phys. Rev. Lett.* **85**, 888–891 (2000).
43. P. A. Smith, G. Petekidis, S. U. Egelhaaf, W. C. K. Poon, Yielding and crystallization of colloidal gels under oscillatory shear. *Phys. Rev. E* **76**, 041402 (2007).
44. S. W. Kamp, M. L. Kilfoil, Universal behaviour in the mechanical properties of weakly aggregated colloidal particles. *Soft Matter* **5**, 2438–2447 (2009).

45. P. Bartlett, L. J. Teece, M. A. Faers, Sudden collapse of a colloidal gel. *Phys. Rev. E* **85**, 021404 (2012).
46. T. Gibaud, D. Frelat, S. Manneville, Heterogeneous yielding dynamics in a colloidal gel. *Soft Matter* **6**, 3482 (2010).
47. J. H. B. Sprakel, S. B. Lindström, T. E. Kodger, D. A. Weitz, Stress Enhancement in the Delayed Yielding of Colloidal Gels. *Phys. Rev. Lett.* **106**, 248303 (2011).
48. M. Leocmach, C. Perge, T. Divoux, S. Manneville, Creep and fracture of a protein gel under stress. *Phys. Rev. Lett.* **113**, 038303 (2014).
49. V. Grenard, T. Divoux, N. Taberlet, S. Manneville, Timescales in creep and yielding of attractive gels. *Soft matter* **10**, 1555–71 (2014).
50. S. M. Klein, V. N. Manoharan, D. J. Pine, F. F. Lange, Preparation of monodisperse PMMA microspheres in nonpolar solvents by dispersion polymerization with a macromonomeric stabilizer. *Colloid Polym. Sci.* **282**, 7–13 (2003).
51. G. Bosma, C. Pathmamanoharan, E. H. A. de Hoog, W. K. Kegel, A. van Blaaderen, H. N. Lekkerkerker, Preparation of monodisperse, fluorescent PMMA-latex colloids by dispersion polymerization. *J. Colloid Interface Sci.* **245**, 292–300 (2002).
52. C. P. Royall, A. A. Louis, H. Tanaka, Measuring colloidal interactions with confocal microscopy. *J. Chem. Phys.* **127**, 044507 (2007).
53. W. C. Poon, E. R. Weeks, C. P. Royall, On measuring colloidal volume fractions. *Soft Matter* **8**, 21 (2012).
54. C. P. Royall, M. E. Leunissen, A. v. Blaaderen, A new colloidal model system to study long-range interactions quantitatively in real space. *J. Phys.: Condens. Matter* **15**, S3581-S3596 (2003).
55. M. Leocmach, Colloids **doi:10.5281/zenodo.31286** (2009).
56. A. a. Hagberg, D. a. Schult, P. J. Swart, *Proceedings of the 7th Python in Science Conference*, J. Millman, G. Varoquaux, T. Vaught, eds. (2008), vol. 836, pp. 11–15.

Acknowledgements:

Funding: This study was partly supported by Grants-in-Aid for Scientific Research (S) (21224011) and Specially Promoted Research (25000002) from the Japan Society of the Promotion of Science (JSPS). Collaboration between M.L. and H.Tanaka has been funded by CNRS through Projet international de coopération scientifique No 7464. M.L. acknowledges support from ANR grant GelBreak ANR-17-CE08-0026. J.R. acknowledges support from the European Research Council Grant DLV-759187 and the Royal Society University Research Fellowship.

Author Contributions H.Tsurusawa and M.L. contributed equally to this work. H.Tanaka conceived and supervised the project. H.Tsurusawa performed experiments. M.L. performed all the analysis of the experimental coordinates. J.R. performed simulations. M.L., J.R. and H.Tanaka discussed and wrote the manuscript.

Competing Interests The authors declare that they have no competing financial interests.

Data and materials availability: Additional data and materials are available online.

Supplementary Information

Direct link between mechanical stability in gels and percolation of isostatic particles.

Hideyo Tsurusawa,¹ Mathieu Leocmach,² John Russo,¹ Hajime Tanaka^{1*}

¹Department of Fundamental Engineering, Institute of Industrial Science, University of Tokyo,
4-6-1 Komaba, Meguro-ku, Tokyo 153-8505, Japan

²Univ Lyon, Université Claude Bernard Lyon 1, CNRS, Institut Lumière Matière,
F-69622, Villeurbanne, France

³School of Mathematics, University of Bristol, Bristol BS8 1TW, United Kingdom

*To whom correspondence should be addressed; E-mail: tanaka@iis.u-tokyo.ac.jp.

Semi-permeable cell and protocol

Gelation of micron-size colloids suitable for quantitative confocal microscopy is usually induced by depletion attractions due to polymers in the solvent. The experimental protocols that have been used so far for studying the kinetics of phase separation and gelation are as follows: (1) Colloidal suspensions saturated with salt and polymer solutions are mixed just before an experiment, and after mixing transferred to a capillary tube as quickly as possible. (2) A mixture of colloids, polymers, salt, and solvents, which is already in a final state point in the phase diagram and intrinsically unstable, or phase-separated, is vigorously stirred just before an experiment to break pre-existing phase separated structures by shear melting. However, these protocols have two common serious deficiencies. Firstly the initial state can never be homogeneous perfectly, and so there already exist particle aggregates at $t = 0$. Secondly, the mixing inevitably involves turbulent flow, which does not decay but remains when the observation is initiated. The gelation process observed by these conventional protocols inevitably suffers from the influence of ill-defined initial static and dynamic conditions, and it has been almost impossible to access the very initial stage of gelation without interference of pre-existing aggregates and/or turbulent flow.

We overcome these limitations as follows. We use a colloidal system that is charge stabilised at long range, has a short range depletion attraction, and is also sterically stabilised caus-

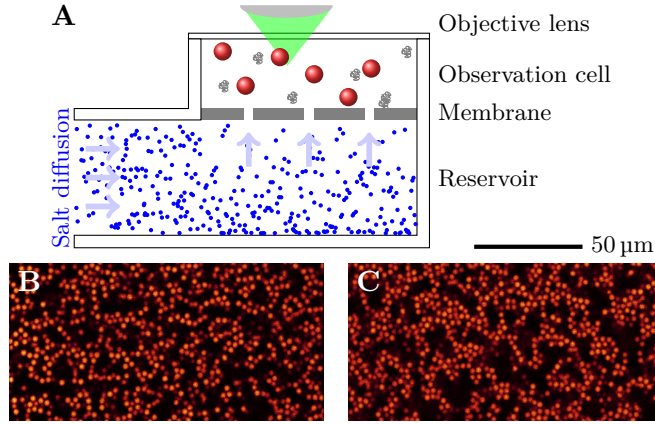


Fig. S1: Reservoir cell. (A) Sketch of our experimental setup. The observation cell contains initially colloids, polymer and no salt. (B) Confocal slice of a gel formed *in situ* by our method ($\phi = 25.5\%$, $c_p = 1.4$ mg/g), 1 hour after gelation. (C) Idem for a gel at the same state point formed *ex situ* and immediately pumped into a capillary.

ing nearly hard sphere repulsion at contact. We disperse colloidal particles and non-adsorbing polymers in a mixture of organic solvents that matches both the refractive index and the density of the particles. The ratio of the two solvent is first adjusted at 37°C to match the density of our particles. Even more precise matching is then obtained by adjusting the temperature. By this method, we realize a density matching of the order of 10^{-4} between the density of the colloids and of the solvent, enough to observe the late stage of gelation with little influence of gravity despite our large particle size (gravitational Peclet number $\text{Pe} < 10^{-6}$). Because of the weakly polar nature of the solvent mixture (its dielectric constant $\epsilon_r = 5 \sim 6$), the Debye screening length is about $\kappa^{-1} = 10\ \mu\text{m}$, long enough for the large colloids (diameter $\sigma = 2.75\ \mu\text{m}$) to form a homogeneous Wigner crystal in the mixture (1). The short ranged ($\sim \sigma/10$), depletion attraction caused by the polymers is masked by the electrostatic repulsion.

The colloids and polymers are contained in an observation cell ($10\ \text{mm}^2 \times 200\ \mu\text{m}$) made of glass in contact with an half-open glass channel approximately 400 times larger in volume, via a millipore filter with pore size of $100\ \text{nm}$ that allows the salt through but neither polymer nor colloid (see Fig. S1(A)). The channel is filled with the same solvents at density matching composition. At the beginning of the experiment, solid tetrabutylammonium bromide (Fluka) is introduced to the channel. Data acquisition starts within 30 s after salt introduction. Our procedure induces practically no solvent flow in the observation cell. We confirmed the presence of undissolved salt several days after mixing, indicating that the observation cell was brought to saturation concentration.

Given the diffusion constants of Bromide and alkyl cation (6 and $2 \times 10^{-10}\ \text{m}^2\ \text{s}^{-1}$ (2)), we estimate the characteristic diffusion time of salt from top to bottom of the order of 10 s. Therefore, we reach uniform final salt concentration into the observation cell within only a

few Brownian times of the colloids. Indeed we measured a delay of about 1 min between the aggregation at the bottom and at the top of the cell. We define the initiation time of the aggregation process when the maximum of the $g(r)$ jumps from the lattice constant of the Wigner crystal to the hard-core diameter σ .

We collect the data on a Leica SP5 confocal microscope, using 532 nm laser excitation. The temperature was controlled on both stage and objective lens, allowing a more precise density matching. The scanned volume is at least $82 \times 82 \times 85 \mu\text{m}^3$. The particle coordinates are tracked in three dimensions (3D) with an accuracy of around 0.03σ (3).

Figure S1(B) and (C) compare the final structures of two gels prepared at the same state point with the two different protocols: the first one by our salt-injection protocol, and the latter by the conventional approach, where a gel is formed in a capillary and then shear melted at the start of the experiment. Already a visual inspection reveals that the latter is coarser, highlighting that shaking or shear melting protocols (4, 5) are not equivalent to a quench. Our special quench protocol provides an ideal experimental platform to make a comparison with theory and simulations. However, we note that Brownian Dynamics simulations cannot reproduce our experimental results even with the same quench, because they neglect the solvent mediated hydrodynamic interactions (6, 7).

Spinodal decomposition dynamics

To confirm whether the different samples follow spinodal-decomposition kinetics, we compute the time dependent static structure factor $S(q, t)$. Our experimental data do not have periodic boundary conditions, so we must use a window function to ensure the correct correlation, especially at small q . Here we use the Hanning window, that significantly affects only the values of $S(q)$ at the first lowest five q that we discard in the rest of the analysis. We checked that our results are not affected by other reasonable choices of the window function.

For all gel and cluster samples, we observe the appearance of a low q peak in $S(q)$, see Fig. S2, which is characteristic of spinodal decomposition in a system with a conserved order parameter.

The characteristic wave number is defined as

$$\langle q \rangle = \frac{\int_0^{q_{\min}} dq q S(q)}{\int_0^{q_{\min}} dq S(q)}, \quad (1)$$

where q_{\min} is fixed at all times at a value that corresponds to the minimum between the low- q peak and the hard sphere peak. The temporal evolution of $\langle q \rangle$ is shown on Fig. S3 for various colloidal volume fractions. The curves for all samples follow a master curve coherent with spinodal decomposition kinetics: At short times $\langle q \rangle(t)$ shows a plateau indicating that the low q peak builds up at a constant wave number corresponding to distances of about 2σ . This plateau is characteristic of the early stage spinodal decomposition, which is described by Cahn's linear theory (8). At intermediate times, on the other hand, we observe coarsening with $\langle q \rangle \sim t^{-\alpha}$,

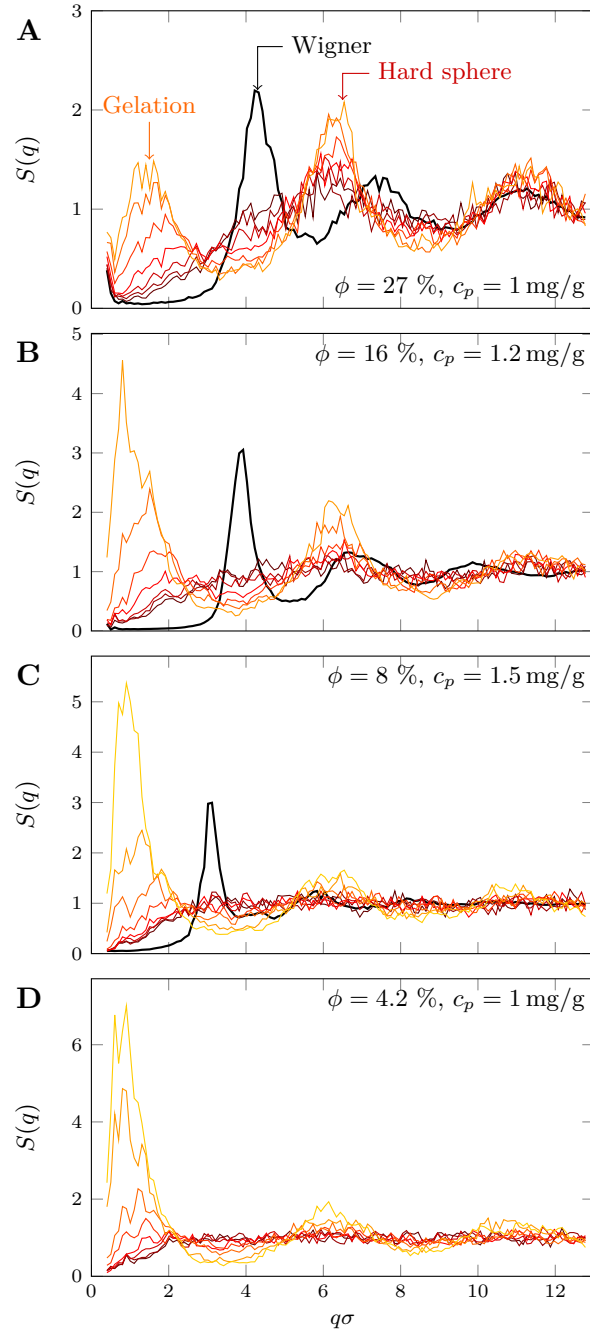


Fig. S2: Temporal change of the structure factor. Panels (A-D) are for the four samples shown on Fig. 2 of the main text by decreasing volume fraction: $(\phi, c_p) = (27\%, 1 \text{ mg/g})$, $(16\%, 1.2 \text{ mg/g})$, $(8\%, 1.5 \text{ mg/g})$, and $(4.2\%, 1 \text{ mg/g})$, respectively. The thick black curve corresponds to the initial Wigner crystal before salt introduction (ill defined thus not shown in (D)). Thin curves from dark red to yellow are spaced by 150 s and display a peak corresponding to the hard sphere diameter as well as a growing peak at low q indicating phase separation.

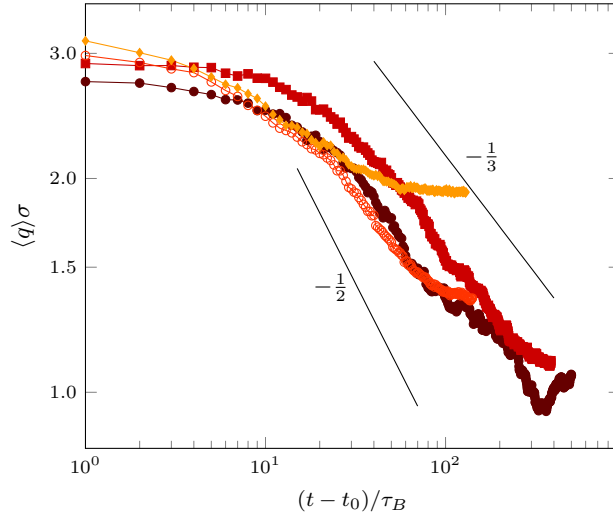


Fig. S3: Temporal change in the characteristic wave number. The symbols, \blacklozenge , \circ , \blacksquare and \bullet , represent data at $\phi = 4.2, 8, 16, 27\%$, $c_p = 1, 1.5, 1.2, 1$ mg/g, respectively. The lines are possible scaling laws for the intermediate coarsening regime.

with an exponent α which is compatible with both $\alpha = 1/3$, typical of spinodal decomposition without dynamical asymmetry between the two phases, and $\alpha = 1/2$, which is often observed in viscoelastic phase separation (see, e.g., Ref. (6)). Due to the narrow range of this power law regime and finite size effects, we cannot conclude definitely on the exponent value. Finally at longer times each sample deviates from the master curve to form a plateau indicating dynamical arrest. The more dilute samples arrest sooner, but reciprocal space information does not allow to identify whether the origin of arrest is different between clusters and percolated networks. This problem can be solved by real-space observation.

Our real-space observations indicate that both the cluster and gel phases are due to viscoelastic spinodal decomposition (9, 10): network-type spinodal for the gel (see Fig. 1), and droplet-type spinodal for the clusters (see Fig. S4), where strong dynamical asymmetry between colloids and the solvent leads to unique roles of hydrodynamics and mechanics in phase separation.

Real space analysis

Characterization of the system.

From direct confocal measurements (11, 12), we estimate the hard-core diameter of our colloids ($\sigma = 2.75 \mu\text{m}$) and the range of the interaction potential (that confirmed our scaling of R_g within 1%), leading to a polymer-colloid size ratio $q = 2R_g/\sigma = 0.10(6)$. The spinodal line

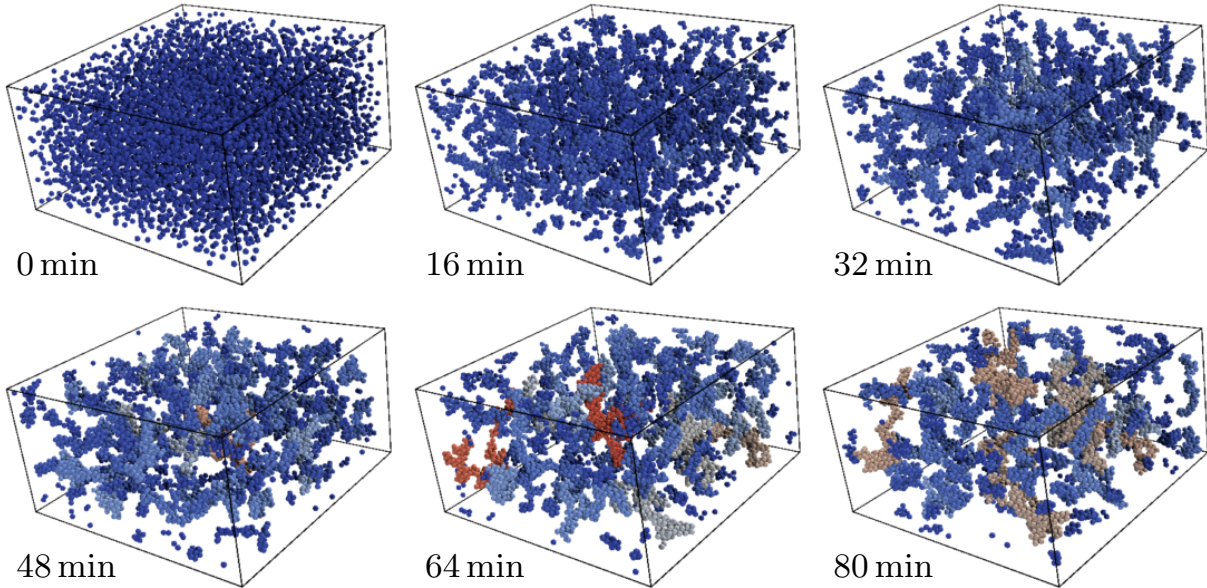


Fig. S4: Cluster phase formation observed by our method. Experimental coordinates are reconstructed and colored by the number of particles in the cluster ($\phi = 4.7\%$, $c_p = 1$ mg/g).

and polymer overlap concentration lines in Fig. 2 are calculated from this size ratio, using the generalized free volume theory (13).

Detection of bonds.

In principle the attraction well of the depletion extends to $\sigma + 2R_g$, however, resolution-dependent tracking imprecision and systematic errors do not give a precise enough estimate of such short distance. Therefore we consider two particles bonded when their distance is shorter than the first minimum distance of $g(r)$, i.e. $3.55\ \mu\text{m}$. This defines the bond graph that we analyse using NetworkX library (14). We have checked that the precise choice of this distance does not affect significantly our results, in particular percolation times. We consider that a bond is effectively broken when it does not reform within $10\tau_B$.

Coordination number analysis.

On the basis of the above definition of bonds, we analysed the evolution of the coordination number of the colloidal particles. The results are shown in Fig. S5. We also study how the gelation path depends on polymer concentration by looking at the growth of the largest cluster size as a function of the average coordination number \bar{N}_c (see Fig. S6).

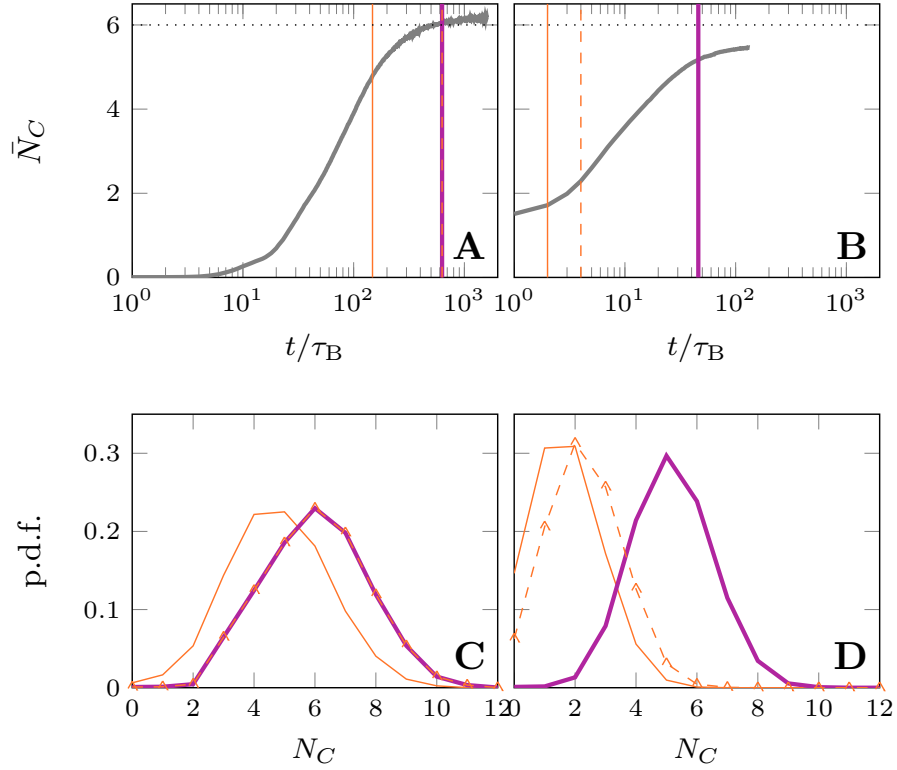


Fig. S5: Coordination number analysis for a dilute ($\phi = 8\%$, $c_p = 1.5\text{ mg/g}$: **A**, **C**) and a dense ($\phi = 27\%$, $c_p = 1\text{ mg/g}$: **B**, **D**) sample. (**A**,**B**) Evolution of the mean coordination number. The thin orange and thick purple vertical lines show the isotropic percolation times for all particles (τ_{IT}^{all}) and isostatic particles (τ_{IT}^{IS}) respectively. The dashed orange vertical line shows the directed percolation time of all particles (τ_D^{all}). (**C**, **D**) Probability distribution of the coordination number at τ_{IT}^{all} (thin orange), τ_D^{all} (dashed orange and triangles) and τ_{IT}^{IS} (thick purple).

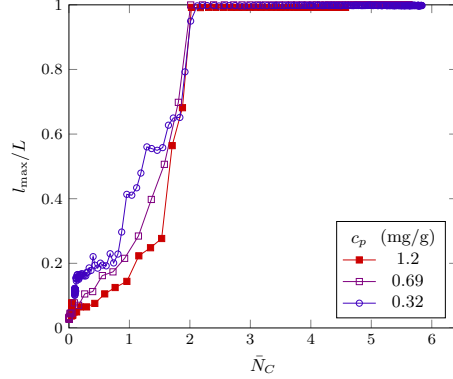


Fig. S6: Gelation path dependence on polymer concentration. Comparison of system evolution in terms of largest cluster extent and of mean coordination number. The symbols, \blacksquare , \square and \circ , represent data at $(\phi, c_p) = (16\%, 1.2 \text{ mg/g})$, $(15\%, 0.69 \text{ mg/g})$ and $(14\%, 0.32 \text{ mg/g})$, respectively.

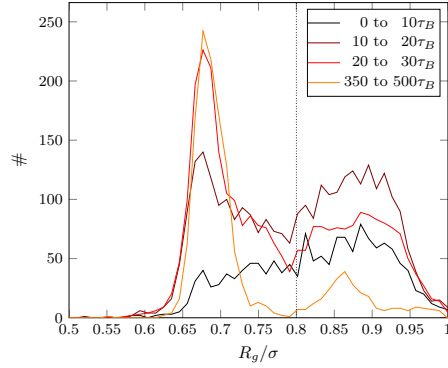


Fig. S7: Evolution of the population of triplets as a function of their radius of gyration. The result is for a non percolating sample ($\phi = 4\%$, $c_p = 1 \text{ mg/g}$).

Role of hydrodynamics

To see the role of hydrodynamics in the process of colloidal phase separation, we follow the compaction of clusters made of only three particles in a non-percolating sample. The time-averaged probability distribution of the radius of gyration R_g of these triplets shows two peaks on both sides of $R_g^* = 0.8\sigma$, see Fig S7. For $R_g < R_g^*$ the cluster is compact, with a structure close to an equilateral triangle. For $R_g > R_g^*$ the three particles are aligned and the cluster is elongated. We found that just after the quench triplets have a slightly higher probability of being elongated. Afterwards, they either connect to other clusters or relax to the more stable compact state. To follow this relaxation, we define the probability to stay elongated as

$$P_{\text{el}}(\Delta t) = \langle P(\delta_i(t + \Delta t) | \delta_i(t)) \rangle_{t,i}, \quad (2)$$

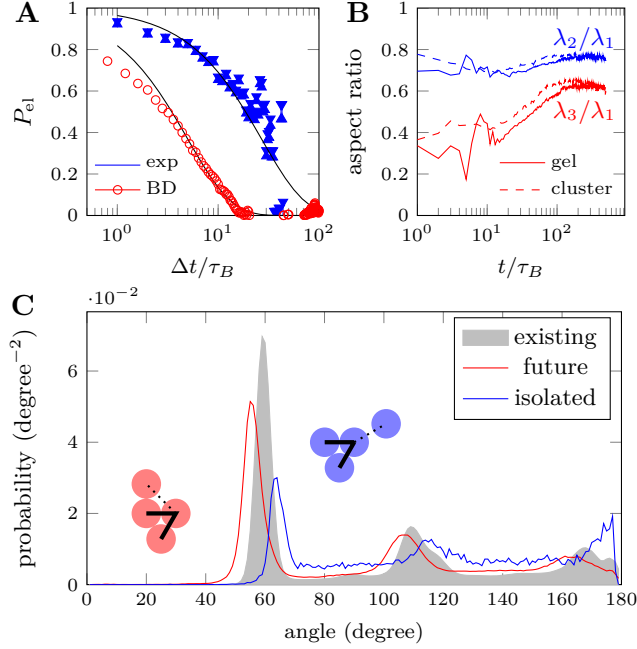


Fig. S8: Role of hydrodynamics on colloidal phase separation. **(A)** Probability of staying elongated for a triplet in a non-percolating sample ($\phi = 4\%$, $c_p = 1$ mg/g, blue) and in corresponding BD simulations. The continuous lines are the respective best exponential fits of characteristic time $27\tau_B$ and $5\tau_B$ respectively. **(B)** Evolution of the aspect ratios of clusters of 4 particles and more in the same sample (dashed lines) and in a percolating sample ($\phi = 8\%$, $c_p = 1.5$ mg/g, continuous lines). **(C)** Bond angle distribution relative to existing bonds (grey), to a future bond (red) or to a future bond involving an isolated particle (blue) obtained in the percolating sample. Future bonds are shifted to smaller angles, whereas gas adsorption takes place from larger angles. Insets sketch both cases, with present bonds drawn thick and future bonds drawn dotted.

where $\delta_i(t) = 1$ when the triplet i is elongated at time t and $\delta_i(t) = 0$ otherwise. Figure S8(A) (blue line) shows that the decay of $P_{\text{el}}(\Delta t)$ is exponential with a characteristic time of $27\tau_B$. In the same figure we also plot (red symbols) the same quantity computed from Brownian Dynamics simulations of short-range attractive colloids designed to match the experiments (see below), in which the triplet compaction process is simulated in absence of hydrodynamic interactions. For the simulations we observe a considerably faster exponential decay compared to the experiments, suggesting that the triplet compaction process is indeed slowed down significantly by hydrodynamic interactions.

Simulations To simulate the process of triplet compaction in absence of hydrodynamic interactions, we use Langevin dynamic simulations, where the characteristic damping time of the velocities τ_D is chosen to be equal to the Brownian time τ_B , i.e. the time it takes a colloid to diffuse its diameter. We use a generalised LJ potential (with exponent $n = 100$ and interaction strength $\epsilon = 8k_B T$) chosen to match the second virial coefficient of the Asakura-Osawa potential corresponding to experimental conditions (the ratio of polymer to colloid diameter, $q = 0.1$ and strength $\epsilon = 8k_B T$). Following Ref. (4), the process of matching the second virial coefficient should ensure equivalent dynamical behavior for all short-range potentials. The elongation probability Eq. (2) is computed by running two hundred independent simulations and measuring the statistics of open and compact configurations of the triplets.

The shape of clusters composed of more than 3 particles cannot be followed in the same way. Instead, we compute the principal moments of gyration of individual clusters λ_j , ordered such that $\lambda_1 \geq \lambda_2 \geq \lambda_3$, with use the aspect ratios λ_2/λ_1 and λ_3/λ_1 to quantify the departure from sphericity. In Fig. S8(B), we show the evolution of the average value of these aspect ratios either for a non-percolating sample (dashed line), or before percolation for a percolating one (continuous line). In both cases, we observe that the clusters are originally not compact and become more isotropic over tens of τ_B . As can be seen in Fig. 1 and Fig. S4, structural isotropy is recovered only after the fusion of many anisotropic clusters into a branched structure that may or may not be percolating.

These observations can be understood as due to hydrodynamic effects. Indeed in a solvent, particles cannot converge freely to form compact structures (6,9). The compaction is delayed by the incompressibility of the solvent, which allows only divergence-free transverse flow fields. Furthermore, clusters influenced by hydrodynamic interactions tend to be more elongated, less compact. We can test this hypothesis by measuring at which angle particles meet relative to existing neighbors. If influenced by hydrodynamics, particles should avoid the direction of existing neighbors and come from more open angles. In Fig. S8(C) we show the bond angle distribution for three different sets of bonds: (i) existing bonds, (ii) bonds that will form within the next τ_B (*future bonds*), (iii) future bonds where the newly attached particle is a monomer. As expected, existing bonds (i) are preferentially at a 60° angle, indicating stable packing, with secondary peaks coherent with a mixture of tetrahedral and hexagonal packing. Future bonds (ii) have more acute angles and almost never 180° , since they are mostly due to particles

attached to second neighbors, see sketch in Fig. S8(C). Here hydrodynamics plays no role. By contrast, future bonds (iii) involving isolated particles form at more obtuse angles, with a clear peak around 180° . This confirms that hydrodynamics has a significant influence on particle aggregation and explains why clusters are initially elongated.

Consequently, long-lived elongated clusters have a higher probability to meet via either rotational or translational diffusion than compact spherical clusters. Hydrodynamics explains why in a rather dilute regime we can observe immediate formation of elongated clusters and then their slow, hydrodynamically-assisted aggregation into a percolated structure. We stress that this is a direct consequence of large-size disparity between colloidal particles and solvent molecules, which leads to the physical situation where discrete solid objects are floating in a continuum liquid.

Estimation of the internal stress.

We measure $k_D(t)$, the bond breaking rate at time t , by counting how many bonds have been broken between t and $t + \tau_B$ and dividing by the total number of bonds at t . The resulting rates are averaged on a window whose size is increased exponentially with $t - t_0$. In this way at short times the values of $k_D(t)$ are instantaneous, while at long times we ensure good statistics despite the low count of breaking events every τ_B .

To extract internal stresses from $k_D(t)$ measurements, we model the bond breaking rate using a Kramers approach (15). In absence of force \mathcal{F} acting on a bond, the dissociation rate is

$$k_D(\mathcal{F} = 0) = \omega_0 \exp\left(-\frac{E_A}{k_B T}\right), \quad (3)$$

where E_A is the depth of the potential and ω_0 an attempt frequency that depends on the precise shape of the potential (16) and on the diffusion constant in the depletion shell (17). Under action of small force \mathcal{F} , the rate becomes (18)

$$k_D(\mathcal{F}) = k_D(\mathcal{F} = 0) \exp\left(\frac{\mathcal{F}\delta}{k_B T}\right) \quad (4)$$

with δ the width of the potential, here twice of the gyration radius of polymer, $2R_g$. If we can measure k_D in absence of force, we can obtain the force at all times:

$$\mathcal{F}(t) = \frac{k_B T}{\delta} \log \frac{k_D(t)}{k_D(\mathcal{F} = 0)}. \quad (5)$$

We convert the force into the internal stress Σ using the area of contact between depletion shells $\Sigma = 2\mathcal{F}/(\pi\sigma\delta)$. Here we measure $k_D(\mathcal{F} = 0)$ by supposing that at long times, once hydrodynamic stresses can be neglected, local rearrangements of the network are force-free, that is when the involved particles keep a common neighbor after bond breaking, the long time limit of the blue curve in Fig. S9.

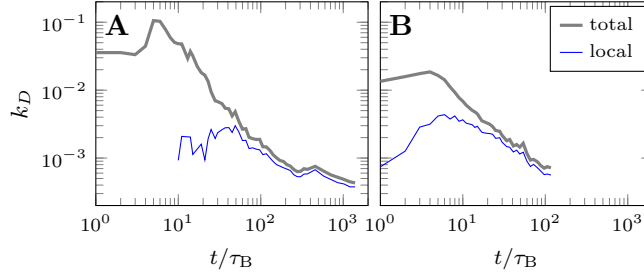


Fig. S9: Bond breaking rates for a dilute **(A)** ($\phi = 8\%$, $c_p = 1.5$ mg/g) and a dense **(B)** ($\phi = 27\%$, $c_p = 1$ mg/g) percolating sample. The thick grey curve shows the total breaking rate. The thin blue curve counts only breaking events after which the two particles still have a common neighbor.

Microrheological measurements of viscoelasticity.

We perform two-particle microrheology following Ref. (19). Briefly, we compute the two-point mean square displacement $\langle \Delta r^2 \rangle_D(t, \Delta t)$, averaged over all couples of particles (i, j) so that $2\sigma < r_{ij} < r_{\max}$ and particle i is further away than r_{\max} from any edge of the observation window. We chose r_{\max} as the fourth of the shortest dimension of the observation window. Using a generalised Stokes-Einstein relation, we obtain the complex modulus

$$G(\omega, t) = G'(\omega, t) + iG''(\omega, t) = |G(\omega, t)|e^{i\delta(\omega, t)}. \quad (6)$$

In a first order approximation, the loss angle $\delta(\omega, t)$ is directly linked to the logarithmic derivative of the mean square displacement

$$\alpha(\Delta t = \omega^{-1}, t) = \frac{d \log \langle \Delta r^2 \rangle_D}{d \log \Delta t} \approx \frac{2}{\pi} \delta(\omega, t) \quad (7)$$

Following Ref. (20), we analyse the various sources of errors in our microrheology measurements. Static errors on tracked coordinate affect the magnitude of the complex modulus $G(\omega, t)$, but never its phase $\delta(\omega, t)$. In other words, the ratio G''/G' , also called loss tangent $\tan \delta$, is robust to static errors. Dynamic errors can occur due to the finite exposure time τ_{expo} and can in principle affect the loss tangent. If the mean square displacement can be locally approximated by a power law of exponent $\alpha > 0$ function of Δt , Savin and Doyle (20) have expressed the MSD affected by dynamic errors function of $\tilde{\tau} = \Delta t / \tau_{\text{expo}}$. Using this expression and (Eq. (7)), we derive the resulting relative error on $\delta(\omega, t)$ as

$$\frac{|\Delta \delta|}{\delta}(\omega, t) \approx \frac{(\omega \tau_{\text{expo}})^{2\delta/\pi}}{(1 + \frac{2\delta}{\pi})(1 + \frac{\delta}{\pi})}. \quad (8)$$

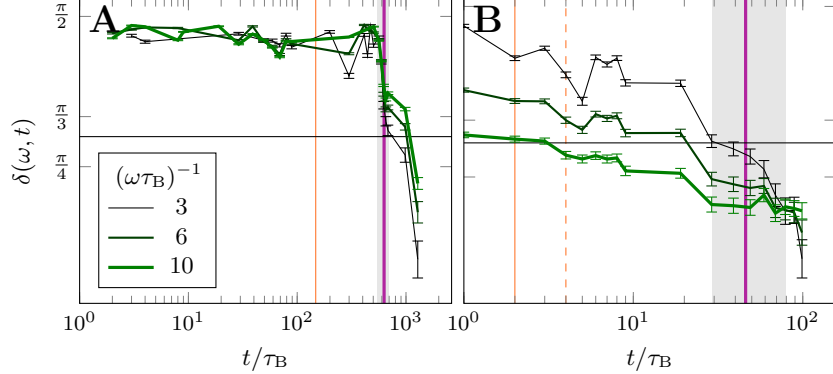


Fig. S10: Temporal change in loss angle. Time evolution of $\delta(\omega, t)$ for three frequencies, for a dilute (**A**) ($\phi = 8\%$, $c_p = 1.5$ mg/g) and a dense (**B**) ($\phi = 27\%$, $c_p = 1$ mg/g) sample. Error bars are estimated from (Eq. (8)). The thin orange and thick purple vertical lines show the isotropic percolation times for all particles (t_{perco}) and isostatic particles (t_6) respectively. The dashed orange vertical line shows the directed percolation time (t_D). The solid horizontal line marks the criterion $\tan \delta(\omega, t) = 1.5$. The grey vertical band lies between the time when the above criterion is satisfied by the highest available frequency and the crossing of all three frequencies.

When $G'' \approx G'$, we also have $\tan \delta \approx 1$ and (Eq. 8) reduces to

$$\frac{|\Delta\delta|}{\delta}(\omega, t) \approx \frac{8}{15} \sqrt{\omega\tau_{\text{expo}}}. \quad (9)$$

In a laser scanning confocal microscope, the exposure time for each particle is only a fraction of the time needed to acquire a full time step. With our experimental parameters, the volume of a single particle is scanned in $\tau_{\text{expo}} \approx 0.3$ s, thus at our highest frequency $\omega\tau_{\text{expo}} \approx 10^{-2}$ and the relative error on the phase is about 5%. This is smaller than the error coming from the definition of gelation point itself.

In general the crossing of G' and G'' depends on the frequency. That is why the gel point is defined as the time when G' and G'' both scale as identical power laws of frequency which corresponds to a loss tangent $\tan \delta = G''/G'$ independent of frequency (21). In Fig. S10 we shows the evolution of the loss angle $\delta = \arctan(G''/G')$ in the two same samples as Fig. 3, for three frequencies. Depending on the sample, the gelation point can be earlier or later than the crossing point of G' and G'' at the highest available frequency. We consider that the time of mechanical gelation τ_{gel} lies between the time when $\tan \delta$ fall below 1.5 at the highest available frequency and the convergence time of the loss angle across all frequencies. On Fig. 3 and Fig. S10, we materialize this range by a vertical grey zone. We confirmed that for all samples $\tau_{\text{IT}}^{\text{IS}}$ the isotropic percolation of isostatic particles fall into this range. Furthermore, in dense samples $\tau_{\text{IT}}^{\text{all}}$, the directed percolation time of all particles, lies well outside of the error bars of τ_{gel} .

Characterisation of the degree of local stretching.

To detect local 2-fold symmetry and thus elongation, we use the following Steinhardt bond orientational order parameter (22, 23) for particle i ,

$$q_2(i) = \sqrt{\frac{4\pi}{5} \sum_{m=-2}^2 |q_{2,m}(i)|^2}, \quad (10)$$

$$q_{2,m}(i) = \frac{1}{N_i} \sum_{j=1}^{N_i} Y_{2,m}(\theta(\mathbf{r}_{ij}), \phi(\mathbf{r}_{ij})), \quad (11)$$

where the $Y_{\ell,m}$ are spherical harmonics and \mathbf{r}_{ij} is one of the N_i bonds involving particle i .

Supplementary Analysis of isostaticity percolation

We compute the cluster size distribution of all particles at the percolation time, and also the isostatic cluster size distribution at the percolation time of isostaticity. We take into account the finite size of the particles by adding one particle radius to the radius of gyration R_g of each cluster. The normalized cluster size is thus

$$\frac{R_g}{\sigma} + \frac{1}{2} = \frac{1}{\sigma} \sqrt{\frac{1}{s} \sum_{i=1}^s \left| \vec{X}_i - \frac{1}{s} \sum_{i=1}^s \vec{X}_i \right|^2} + \frac{1}{2} \quad (12)$$

where s is the cluster size. In that way a one particle cluster has a size of 0.5σ . In that way the fractal range is extended to small clusters. Figure S11(A) show the resulting cluster size distributions for a dilute gel. At usual percolation time, the central range of cluster sizes exhibit a fractal dimension compatible with diffusion-limited cluster aggregation ($D = 1.85$). Large clusters that have an extent comparable to the experimental window display a compact ($D = 3$) fractal dimension. At small cluster sizes we also observe compactness, consistent with the scenario where compaction at small scales proceeds before diffusion-limited percolation. This signature of the original compaction remains when isostaticity percolates. However larger isostatic clusters exhibit a fractal dimension more compatible with directed percolation ($D = 2.27$). This is consistent with the simultaneity of the isotropic percolation of isostaticity and the directed percolation that is observed in dilute samples, see Fig. 3(A) of the main text. At higher volume fraction, Fig. S11(B) shows that usual percolation is just random ($D = 2.53$) at all cluster sizes. However when isostaticity percolates the cluster size distribution of isostatic clusters displays a fractal dimension compatible with directed percolation ($D = 2.27$). Since we know that directed percolation of the whole network took place before isostaticity percolation, see Fig. 3(B), this observation is consistent with a simple invasion of the network by isostaticity.

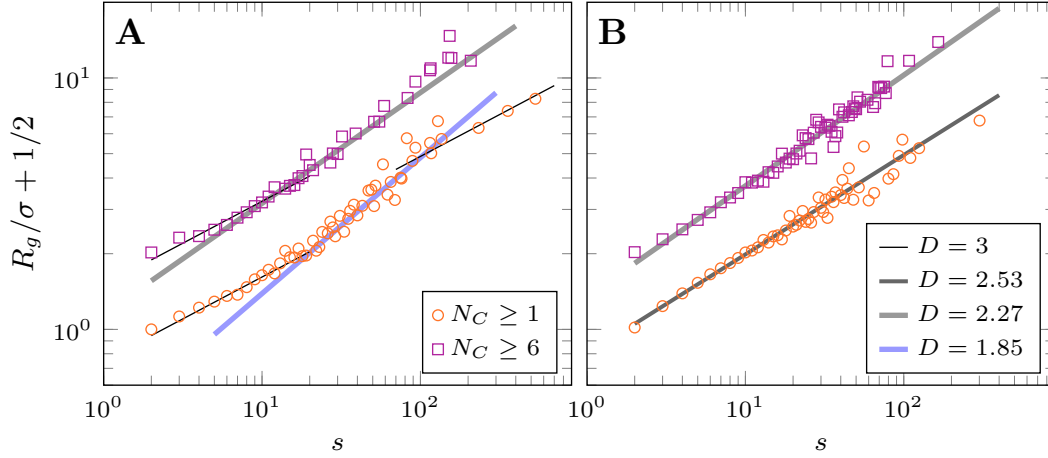


Fig. S11: Cluster size distributions considering either all particles (orange) or isostatic particles (purple), at their respective isotropic percolation time. The later is vertically shifted by a factor 2 for clarity. The thin black lines correspond to a fractal dimension of 3 (compact), dark grey lines to a fractal dimension of 2.53 (random percolation), thick light grey lines to a fractal dimension of 2.27 (directed percolation), and thick light blue lines correspond to a fractal dimension of 1.85 (DLCA). (A) $\phi = 8\%$, $c_p = 1.5$ mg/g. (B) $\phi = 27\%$, $c_p = 1$ mg/g.

To get more insight on the way directed percolation and isostaticity percolation are related in the dilute case, we take a look at what changes as isostaticity invades the network. We take, as a reference, configuration at the percolation time t_{perco} . For low volume fraction gels, local compaction has already occurred at that time, and we detect hundreds of small isostatic clusters that are embedded in a percolated but non isostatic network. We define $\mathcal{X}_i(t)$ the position of the center of mass at time t of the set particles that formed isostatic cluster i at $t = t_{\text{perco}}$. We note $\mathcal{X}_{ij}(t) = |\mathcal{X}_j(t) - \mathcal{X}_i(t)|$ the Euclidian distance between the centers of mass of i and j , and $\Delta\mathcal{X}_{ij}(t) = \mathcal{X}_{ij}(t) - \mathcal{X}_{ij}(t_{\text{perco}})$ its increment. When taking an ensemble average over all pairs of clusters that are not directly connected or far apart in the network $\langle\Delta\mathcal{X}_{ij}(t)\rangle$ is null. However when considering only pairs of clusters that are less than 10 bonds away on the network, we can observe a shortening of the distance between them, see Fig. 4(E). It means that, as loose strands are converted to isostaticity, see Fig. 4(B-D), these strands shorten and straighten. This change in morphology allows longer directed path and thus promotes directed percolation.

Comparison with the work of Kohl et al. (24)

The colloidal system used by Kohl et al. (24) is, within minor details, the same as ours. We do not use the same steric stabilizer or the same dye. One of their solvents is *cycloheptylbromide* where we use *cyclohexylbromide*. They screen electrostatic repulsion using *tetrabutylammonium chloride* where we use *tetrabutylammonium bromide*. Their particles are smaller (diam-

eter of $1.72\ \mu\text{m}$ instead of $2.75\ \mu\text{m}$) and more polydisperse (7% instead of 4-5 %). Relative to the particle size, their polymer is also smaller, with a size ratio of $q = 2R_g/\sigma = 0.076$ in their case but 0.10 in our case. Despite the difference in these details, both their and our experiments are in the limit of sticky spheres with a combination of both depletion attraction and negligible Coulombic repulsion. We do not expect any fundamental differences from these experimental variations, although the precise localization of the spinodal line, of the isotropic percolation line, and of the directed percolation line should be different. We did not compute the localization of the percolation lines in our case as our conclusions rely on a different set of evidence.

Once scaled by the particle size, our field of view is comparable to theirs (largest dimension of $\approx 30\sigma$), although our window is cubic whereas theirs is half as thin as large. Our frame rate is higher in the absolute value and even more so once scaled by the Brownian time. They acquire a 3D image every $6\tau_B$ where we acquire every τ_B . These differences ensure our definitions of percolation that are less dependent on the direction and a better understanding of fast dynamics.

The first important experimental difference is that Kohl et al. observe only their sample at a rather late stage, once all percolations have fully developed, whereas we observe the full process of gelation from a well defined initial state. It is well known that the structure of a gel can be tuned by its shear history (25, 26). However, without measurements during the sample introduction protocol of Kohl et al., we cannot quantify the influence of that process on the final gel structure.

The second important difference is that Kohl et al. have focused both their experiments and their simulations on a low polymer volume fraction regime $\phi \approx 0.2$ and varied both polymer concentration and salt concentration. In particular, their simulations allow much higher salt concentrations than what is possible experimentally. We have not explored the salt concentration axis, however we have varied the volume fraction from 6 to 33%. It is on that axis, at high volume fraction, that we find the discrepancy between τ_D^{all} and $\tau_{\text{IT}}^{\text{IS}}$. At low volume fraction, directed percolation of all particles and isotropic percolation of isostatic particles are simultaneous. Therefore the conclusion of Kohl et al., that rigidity comes with directed percolation, is coincidentally correct *in the narrow range of polymer volume fraction they explored*. We demonstrate that a more general criterion is the isotropic percolation of isostatic particles.

Supplementary Movie 1 Reconstructions from confocal coordinates of the whole process of gelation at $\phi = 7.7\ \%$, $c_p = 1\ \text{mg/g}$. The phase separation is induced by salt injection. Particles are drawn to scale, and colored according to the radius of gyration of the cluster they belong to. Time stamp is $(t - t_0)/\tau_B$. We can see that there is little macroscopic flow in this protocol.

Supplementary Movie 2 Reconstructions in a thin slice from confocal coordinates of the whole process of gelation at $\phi = 27\ \%$, $c_p = 1\ \text{mg/g}$. The depth of view is $7.5\ \mu\text{m}$, while the lateral dimension is $140\ \mu\text{m}$. Isostatic particles are drawn to scale, non isostatic ones are drawn smaller for clarity. The bond network is displayed in orange. Time stamp is $(t - t_0)/\tau_B$. In

this sample, isotropic percolation occurs at $t = 2\tau_B$, directed percolation at $4\tau_B$ and isostaticity percolation at $46\tau_B$.

References

1. C. L. Klix, C. P. Royall, H. Tanaka, Structural and Dynamical Features of Multiple Metastable Glassy States in a Colloidal System with Competing Interactions. *Phys. Rev. Lett.* **104**, 165702 (2010).
2. A. I. Campbell, V. J. Anderson, J. S. van Duijneveldt, P. Bartlett, Dynamical arrest in attractive colloids: The effect of long-range repulsion. *Phys. Rev. Lett.* **94**, 208301 (2005).
3. M. Leocmach, Colloids [doi:10.5281/zenodo.31286](https://doi.org/10.5281/zenodo.31286) (2009).
4. P. J. Lu, E. Zaccarelli, F. Ciulla, A. B. Schofield, F. Sciortino, D. A. Weitz, Gelation of particles with short-range attraction. *Nature* **453**, 499–503 (2008).
5. P. Bartlett, L. J. Teece, M. A. Faers, Sudden collapse of a colloidal gel. *Phys. Rev. E* **85**, 021404 (2012).
6. A. Furukawa, H. Tanaka, Key Role of Hydrodynamic Interactions in Colloidal Gelation. *Phys. Rev. Lett.* **104**, 245702 (2010).
7. Z. Varga, G. Wang, J. W. Swan, The hydrodynamics of colloidal gelation. *Soft Matter* **11**, 9009–9019 (2015).
8. A. Onuki, *Phase Transition Dynamics* (Cambridge Univ. Press, Cambridge, 2002).
9. H. Tanaka, Viscoelastic model of phase separation in colloidal suspensions and emulsions. *Phys. Rev. E* **59**, 6842–52 (1999).
10. H. Tanaka, Viscoelastic phase separation. *J. Phys.: Condens. Matter* **12**, R207-R264 (2000).
11. C. P. Royall, A. A. Louis, H. Tanaka, Measuring colloidal interactions with confocal microscopy. *J. Chem. Phys.* **127**, 044507 (2007).
12. W. C. Poon, E. R. Weeks, C. P. Royall, On measuring colloidal volume fractions. *Soft Matter* **8**, 21 (2012).
13. G. J. Fleer, R. Tuinier, Analytical phase diagrams for colloids and non-adsorbing polymer. *Adv. Colloid Interface Sci.* **143**, 1–47 (2008).
14. A. a. Hagberg, D. a. Schult, P. J. Swart, *Proceedings of the 7th Python in Science Conference*, J. Millman, G. Varoquaux, T. Vaught, eds. (2008), vol. 836, pp. 11–15.

15. H. Kramers, Brownian motion in a field of force and the diffusion model of chemical reactions. *Physica* **7**, 284–304 (1940).
16. M. Plischke, B. Bergersen, *Equilibrium Statistical Physics* (WORLD SCIENTIFIC, 2006).
17. P. A. Smith, G. Petekidis, S. U. Egelhaaf, W. C. K. Poon, Yielding and crystallization of colloidal gels under oscillatory shear. *Phys. Rev. E* **76**, 041402 (2007).
18. S. B. Lindström, T. E. Kodger, J. H. B. Sprakel, D. A. Weitz, Structures, stresses, and fluctuations in the delayed failure of colloidal gels. *Soft Matter* **8**, 3657 (2012).
19. J. C. Crocker, M. T. Valentine, E. R. Weeks, T. Gisler, P. D. Kaplan, A. G. Yodh, D. A. Weitz, Two-Point Microrheology of Inhomogeneous Soft Materials. *Phys. Rev. Lett.* **85**, 888–891 (2000).
20. T. Savin, P. S. Doyle, Static and dynamic errors in particle tracking microrheology. *Biophysical journal* **88**, 623–38 (2005). Publisher: Elsevier Citation Key: Savin2005.
21. F. Chambon, H. H. Winter, Linear Viscoelasticity at the Gel Point of a Crosslinking PDMS with Imbalanced Stoichiometry. *J. Rheol.* **31**, 683–697 (1987).
22. P. J. Steinhardt, D. R. Nelson, M. Ronchetti, Bond-orientational order in liquids and glasses. *Phys. Rev. B* **28**, 784–805 (1983).
23. M. Leocmach, Pyboo **doi:10.5281/zenodo.1066568** (2017).
24. M. Kohl, R. F. Capellmann, M. Laurati, S. U. Egelhaaf, M. Schmiedeberg, Directed percolation identified as equilibrium pre-transition towards non-equilibrium arrested gel states. *Nature Commun.* **7** (2016).
25. N. Koumakis, E. Moghimi, R. Besseling, W. C. Poon, J. F. Brady, G. Petekidis, Tuning colloidal gels by shear. *Soft Matter* **11**, 4640–4648 (2015). Citation Key: Koumakis2015.
26. E. Moghimi, A. Jacob, N. Koumakis, G. Petekidis, Colloidal Gels Tuned by Oscillatory Shear. *Soft Matter* (2017).

